

The x-ray flux at the end of the plateau in GRBs 060413, 060607A, and 070110 falls off sharply by a factor $\sim 10^2$. The fall-off occurs at $t \sim 3 \times 10^3$ s and extends over a time $\delta t \sim t$. This steep fall-off requires the accretion time to be sufficiently short, $t_{\text{acc}} \lesssim t/10 \sim 300$ s, which implies that $j_{\text{d},18} \lesssim 3\alpha^{1/3} M_{\text{BH},1}^2$ and $f_{\Omega}(r) \lesssim 0.2\alpha^{1/3}$ at $r \sim 1.5 \times 10^{11}$ (17, 18).

A lower limit for f_{Ω} in the stellar envelope is obtained by the requirement that the in-falling gas should be able to form an accretion disk at the center; this implies that $f_{\Omega} \gtrsim 0.01$. Another constraint comes from the fact that, apart from the flares discussed below, the x-ray LC during the plateau is usually quite smooth. This suggests that t_{acc} is fairly large (which plays the role of a smoothing time scale), and so f_{Ω} is probably not much less than the upper limit of ~ 0.2 .

After the sharp fall-off at the end of the plateau, the LC is expected to decline as $\sim t^{-2}$ if the x-ray emission is dominated by jet luminosity associated with the debris disk (see Eq. 5). However, at these low flux levels the observed x-rays might be dominated by emission from shock-heated circumburst gas (i.e., external shock emission). In this case the flux will decline as $\sim t^{-1}$; e.g., GRB 070110 (Fig. 1).

For those GRBs where the x-ray LC makes a smooth transition at the end of the plateau phase, f_{Ω} should be such that $t_{\text{acc}} \sim t$. For these systems, we require that $f_{\Omega} \sim 0.4$ near the outer edge of the progenitor star.

Rapid flares with short rise times are often seen during the plateau phase of the x-ray LC, and these provide additional constraints. A flare was seen at the beginning of the x-ray plateau in GRBs 060413 and 060607A and at the end of the plateau in GRB 070110 (Fig. 1), with a rise time on the order of $0.1t$. Assuming the flares are produced by a disk instability, the rise time should be a factor of a few larger than the instability time scale t_{inst} . For a viscous instability, $t_{\text{inst}} \sim t_{\text{acc}}$, whereas for a dynamical (e.g., gravitational) instability, $t_{\text{inst}} \sim \Omega_k^{-1} \sim \alpha t_{\text{acc}}$. Taking the flare rise time to be $\sim 5 t_{\text{inst}} \sim 0.1t$, we find that $f_{\Omega} \sim 0.1\alpha^{1/3}$ in the stellar envelope if flares arise as a result of viscous instability, and $f_{\Omega} \sim 0.3$ for a dynamical instability origin for flares. The amplitude of the flare $f_{\text{x,flare}}/f_{\text{x,plateau}}$ can be at most $\sim t_{\text{acc}}/t_{\text{inst}}$. Thus, even in the limit of a dynamical instability, the amplitude is limited to $\sim \alpha^{-1} \sim 10$. Much larger flare amplitudes [for example, in GRB 060526 (5)] might suggest an unusually small value of the viscosity parameter α . Alternatively, these flares may be caused by a sudden increase in the mass fall-back rate, though such an event is not easy to visualize in our model.

The decay time of flares is expected to be on the order of t_{acc} , as this is the time scale on which a transient enhancement of the accretion rate, regardless of its origin, will subside. A noticeable difference between the x-ray plateau and the prompt emission is that LCs are typically more variable during the burst, and this raises a question as to why the central engine behaves differently during the two phases. Part of the difference is that instability time scales are longer when the outer envelope of the star,

with a larger specific angular momentum, is accreted. Another factor is that, during the plateau phase, the jet propagates through an already evacuated cavity and is less prone to fluctuating baryon loading.

An upper limit on the stellar radius R_* is provided by the requirement that the energy expended as the relativistic jet makes its way out of the star not exceed the energy initially injected into the jet. Using results from (19, 20), we find that $R_* \lesssim 5 \times 10^{11}$ cm. Our radius estimates are consistent with this limit.

A possible way to get a handle on the mass of the GRB progenitor star is via the total energy produced in the explosion. The mass accreted during the prompt burst was estimated above to be $\sim 0.5M_{\odot}$. The energy release during the plateau is typically $\sim 10\%$ of that in the prompt burst; that is, $\sim 10^{51}$ erg (assuming the same beaming factor and efficiency as during the initial burst). Therefore, the mass accreted by the BH is only $\sim 0.03M_{\odot}$. Even after allowing for the fact that only a small fraction $\sim (r_d/R_g)^{1/2} \sim 10^{-2}$ of the total fall-back mass actually reaches the BH, the rest being carried away in a disk wind, we estimate that the mass of fall-back gas in the plateau phase is no more than a few M_{\odot} . The mass of the BH can be constrained because much of the mass within $\sim 10^{10}$ cm collapses to the BH; for an evolved star this mass is $\sim 5M_{\odot}$. Thus, we estimate the mass of the GRB progenitor star to be $M_* \sim 10M_{\odot}$, plus whatever mass is ejected in the accompanying supernova explosion, which we are unable to constrain.

Figure 2 summarizes our primary results on the properties of GRB progenitor stars. The three bursts we considered in this paper are notable in that they have a steep fall-off of x-ray flux at the end of the plateau phase. These bursts provide the most detailed information on the properties of their progenitor stars. Many of our arguments and results, especially those in which we use the prompt burst and subsequent steep fall-off to infer the properties of the stellar core, should

apply to any long-duration GRB. Similarly, our discussion of the x-ray plateau can be applied to other bursts that have plateaus in their x-ray LCs that are produced by continuous accretion activity; i.e., those GRBs that show a simple power-law decline of the optical LC and a plateau in the x-ray. These bursts make up roughly one-third of the long GRBs observed by Swift.

References and Notes

1. The possibility of a long-lived central engine activity was suggested (2) soon after the discovery of GRB afterglow emission.
2. J. I. Katz, T. Piran, R. Sari, *Phys. Rev. Lett.* **80**, 1580 (1998).
3. E.-W. Liang, B.-B. Zhang, B. Zhang, preprint available at <http://arXiv.org/abs/0705.1373> (2007).
4. E. Nakar, J. Granot, preprint available at <http://arXiv.org/abs/astro-ph/0606011> (2006).
5. D. N. Burrows *et al.*, *Science* **309**, 1833 (2005); published online 18 August 2005, 10.1126/science.1116168.
6. G. Chincarini *et al.*, preprint available at <http://arXiv.org/abs/astro-ph/0702371> (2007).
7. B. Zhang, *Chin. J. Astron. Astrophys.* **7**, 1 (2007).
8. Y. Fan, T. Piran, *Mon. Not. R. Astron. Soc.* **369**, 197 (2006).
9. A. Panaitescu *et al.*, *Mon. Not. R. Astron. Soc.* **369**, 2059 (2006).
10. S. E. Woosley, *Astrophys. J.* **405**, 273 (1993).
11. B. Paczynski, *Astrophys. J. Lett.* **494**, L45 (1998).
12. The factor of 2 in the expression for t_{th} accounts for the time it takes signals to travel to r and communicate the loss of pressure support at the center.
13. R. Narayan, T. Piran, P. Kumar, *Astrophys. J.* **557**, 949 (2001).
14. K. Kohri, R. Narayan, T. Piran, *Astrophys. J.* **629**, 341 (2005).
15. P. Kumar, R. Narayan, J. L. Johnson, preprint available at <http://arXiv.org/abs/0807.0441> (2008).
16. J. C. McKinney, *Astrophys. J. Lett.* **630**, L5 (2005).
17. The decline of the LC cannot be steeper than $\sim t^{-3}$; this is due to late arriving photons from outside the relativistic beaming angle of Γ^{-1} (18). Therefore, we can only place an upper limit on f_{Ω} from the steepness of the decline after the x-ray plateau.
18. P. Kumar, A. Panaitescu, *Astrophys. J. Lett.* **541**, L51 (2000).
19. E. Ramirez-Ruiz, A. Celotti, M. J. Rees, *Mon. Not. R. Astron. Soc.* **337**, 1349 (2002).
20. C. D. Matzner, *Mon. Not. R. Astron. Soc.* **345**, 575 (2003).
21. S. Vaughan *et al.*, *Astrophys. J.* **638**, 920 (2006).

11 April 2008; accepted 17 June 2008

Published online 26 June 2008;

10.1126/science.1159003

Include this information when citing this paper.

High-Resolution Scanning X-ray Diffraction Microscopy

Pierre Thibault,^{1*} Martin Dierolf,¹ Andreas Menzel,¹ Oliver Bunk,¹ Christian David,¹ Franz Pfeiffer^{1,2}

Coherent diffractive imaging (CDI) and scanning transmission x-ray microscopy (STXM) are two popular microscopy techniques that have evolved quite independently. **CDI promises to reach resolutions below 10 nanometers, but the reconstruction procedures put stringent requirements on data quality and sample preparation.** In contrast, **STXM features straightforward data analysis, but its resolution is limited by the spot size on the specimen.** We demonstrate a ptychographic imaging method that bridges the gap between CDI and STXM by measuring complete diffraction patterns at each point of a STXM scan. The high penetration power of x-rays in combination with the high spatial resolution will allow investigation of a wide range of complex mesoscopic life and material science specimens, such as embedded semiconductor devices or cellular networks.

Imaging techniques that rely on coherence, loosely designated as coherent diffractive imaging (CDI) techniques, have thrived in situations where more traditional modes of mi-

croscopy are difficult to implement. CDI allows high-resolution imaging while eliminating the need to use high-quality lenses, especially hard to produce in the case of x-rays. This experimental

convenience comes, however, at the price of harder data analysis, which often entails reconstructing the image by solving the so-called phase problem. The simplest CDI method, called diffraction microscopy, involves the reconstruction of an image or a three-dimensional (3D) density from far-field diffraction intensities. In the past decade, a number of successful demonstrations of this technique have been reported, ranging from fabricated nanostructures in 2D (1, 2) and 3D (3, 4) to biological specimens in 2D (5, 6). Requirements such as the complete isolation of the specimen have promoted the development of alternative approaches, such as Fourier holography (7, 8) and “ptychography” (9–13). The latter is an experimental method developed in the 1970s for electron microscopy (14), which consists of measuring multiple diffraction patterns by scanning a finite illumination on an extended specimen. Overlap between adjacent illumination positions provides overdetermination in the data. Assuming the profile of the illumination is known, solving the phase problem has been demonstrated to be easier.

Another powerful microscopy technique is scanning transmission x-ray microscopy (STXM). It consists in scanning a focused x-ray beam on a specimen and measuring the transmitted intensity at each raster point. It thus provides a map of the specimen's transmission. Although more advanced imaging modes exist (15, 16), common to all of them is that the resolution is limited by the spot size on the specimen. Increase in resolution thus largely depends on improving focusing optics. STXM relies partly on coherence—higher coherence allows smaller spot sizes—but has developed quite independently from CDI methods.

In this work, we have designed a technique that we call scanning x-ray diffraction microscopy (SXDM), which bridges the gap between scanning microscopy and coherent diffractive methods. To demonstrate this method experimentally, we imaged a buried nanostructure by using a focused hard x-ray beam. The apparatus, described below, is similar to the experimental setups used in both fields. Data acquisition was greatly facilitated by the use of Pilatus, a fast single-photon counting detector having no read-out noise (17). In essence, the experiment follows closely the configuration in which ptychography was first developed. We used a separate reconstruction method (18) to complement the standard STXM analysis tools and reached resolutions about five times higher than the focal spot dimensions. Our algorithmic approach overcomes the main difficulty of ptychographic measurements by automatically recovering the incident illumination profile at the same time as the complex-valued image of the specimen. This feature is critical to obtain high-quality reconstructions because the detailed

structure of the wavefield incident on the specimen is difficult to extract by other means.

A schematic view of the experimental setup is shown in Fig. 1A. An incoming coherent x-ray beam is focused down to a few hundred nanometers on a specimen. The intense focal spot, called the probe, interacts with a small portion of the specimen before propagating out to a pixel array detector in the far-field region. One complete data set is produced by recording diffraction patterns as the specimen is scanned through the focal spot, typically on a 2D grid.

Each measured diffraction pattern carries information on the specimen. More precisely, the wave at the exit of the specimen corresponding to the j th diffraction data set can be expressed as

$$\psi_j(\mathbf{r}) = P(\mathbf{r} - \mathbf{r}_j)O(\mathbf{r}) \quad (1)$$

where $P(\mathbf{r} - \mathbf{r}_j)$ is the probe wavefield translated by a known amount \mathbf{r}_j , and $O(\mathbf{r})$ is the specimen's transmission function, called the object (19). Exit waves ψ_j are called views because they effectively provide information on selected regions of the specimen. Redundancy in the data, needed for ptychographic applications, is enforced with a scanning step size small enough for adjacent views to overlap.

To demonstrate the technique, we measured a SXDM data set, using as a specimen a Fresnel zone plate buried under a gold layer (20). Imaging this type of nanofabricated device demonstrates the penetration power of x-rays and allows a reliable assessment of the resolution and the validity of a reconstruction. The complete data set is a raster scan of 201-by-201 diffraction patterns, produced with a 6.8-keV x-ray beam focused to a 300-nm spot size, each exposed for 50 ms (18). Four of these diffraction patterns are shown in Fig. 1B. These diffraction patterns were sampled on a region of the detector that subtended an angular range of 10 mrad by 10 mrad.

As immediate feedback to the microscopist to define regions of interest, for instance, the SXDM data set can be analyzed by using standard scanning microscopy techniques (15, 16). A simple calculation of the zeroth and first moments of the intensity distribution in each diffraction pattern gives low-resolution images of the transmission and of the gradient of the phase shift produced as the wave traverses the specimen (21).

The result of this STXM analysis on a SXDM data set is shown in Fig. 2, B to D. Whereas the

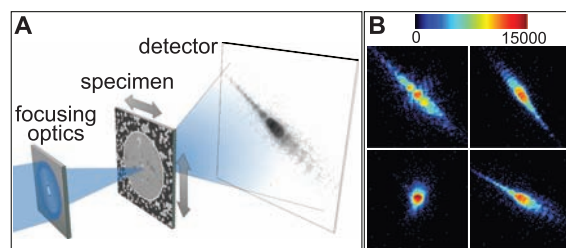
spot size of 300 nm limits the resolution of these preliminary micrographs, it takes on quite a different role in the following analysis, namely, to ensure that the diffraction pattern is sufficiently “oversampled” by the detector in the far field.

The approach we have adopted to reconstruct a high-resolution image from a SXDM data set departs from both earlier methods, that is, the Wigner deconvolution (9, 11) and the ptychographic iterative engine (22, 23). We used the difference map (24), an iterative algorithm now known to have a wide range of applications going far beyond imaging (25). Problems solved by the difference map are formulated as a search for the intersection between two constraint sets. Any solution attempt is represented by a state vector, which typically satisfies neither constraint until the solution is found. For phase retrieval, the state vector generally is a 2D image or a 3D density. For SXDM reconstructions, it is given by the collection of views corresponding to each position of the probe relative to the object. The two constraints on the state vector are the Fourier and the overlap constraints. The former enforces consistency of the views with their corresponding diffraction patterns (26). The latter is given by Eq. 1 and formalizes the redundancy of information in the data set, which gives this algorithm, like related ptychographic techniques (9, 11, 22, 23), its robustness. Projections onto both constraint sets can be precisely defined and easily implemented in a computer program.

At each iteration, the current state is updated through a combination of the two projections, as prescribed by the difference map algorithm. Each computation of the overlap projection yields new estimates of both the probe and the object (27). Unlike many diffraction microscopy reconstructions, this type of problem typically features very short convergence times, a few tens of iterations. It should also be noted that SXDM reconstructions do not suffer from the defocus ambiguity that is met in other CDI methods. The multiplicative relation between the probe and the object ensures that the plane of the reconstruction is well defined.

A reconstruction example, from a 61-by-61 subset of the 201-by-201 diffraction patterns data set, is given in Fig. 3. A second region of interest, closer to the center of the zone plate, is shown in fig. S1. The retrieved complex-valued image provides a map of the optical transfer function of the

Fig. 1. Schematic representation of the experimental setup. (A) The incoming hard x-ray beam is focused on the specimen. A pixel array detector records a complete oversampled diffraction pattern for each raster position of the specimen. (B) Examples of diffraction patterns. The color scale is logarithmic, and the units are in photon counts. The focused beam geometry generates a diverging beam past the specimen, thereby removing the need for a beam stop at the detector.



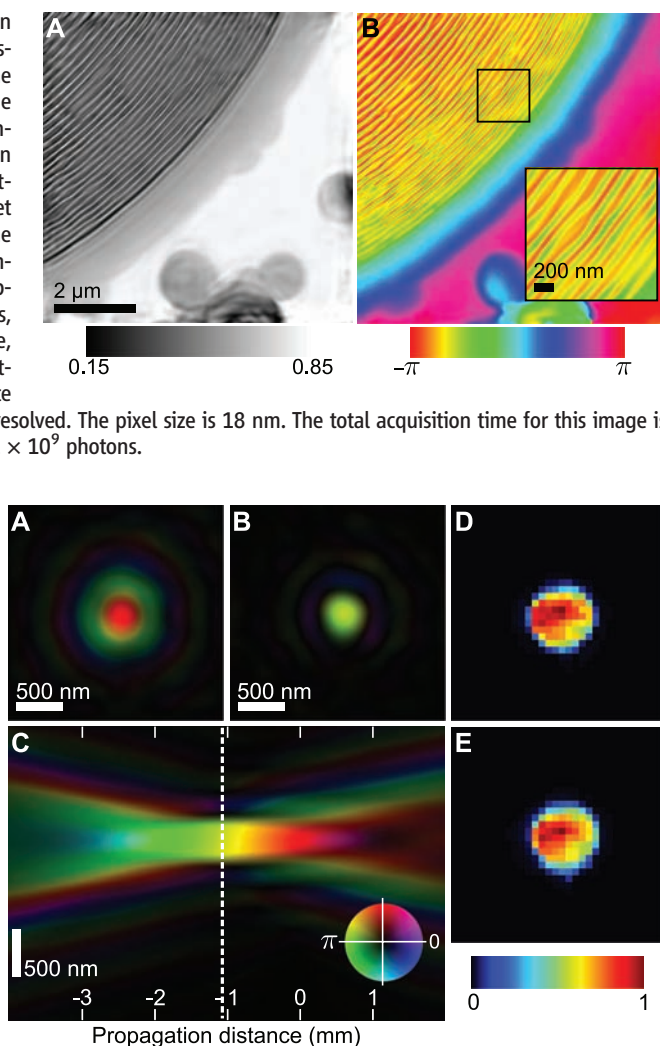
¹Paul Scherrer Institut, 5232 Villigen PSI, Switzerland. ²École Polytechnique Fédérale de Lausanne, 1015 Lausanne, Switzerland.

*To whom correspondence should be addressed. E-mail: pierre.thibault@psi.ch

Fig. 2. Preliminary analysis of a measured data set of 201-by-201 diffraction patterns. This test specimen is a Fresnel zone plate of 30- μm diameter and with 70-nm outer zone width. (A) SEM image. The zone plate structure is completely buried under a layer of gold. A full reconstruction of the region of interest (solid line) is shown in Fig. 3. The reconstructed image of the dashed line region is shown in fig S1. (B) Transmission of the specimen, obtained from the total transmitted intensity at each probe position. (C) Phase gradient of the transmitted wave in the horizontal direction. (D) Phase gradient in the vertical direction. (B) to (D) involve no phase retrieval and can be produced as data are acquired. The pixel size is equal to the scanning grid spacing (100 nm), but the resolution is limited by the size of the probe (about 300 nm).

Fig. 3. SXDM reconstruction of the complex optical transmission function of the zone plate specimen. (A) Amplitude and (B) phase of the reconstruction of a selected region of 61-by-61 diffraction patterns, from the same data set that was used for Fig. 2. The magnified region shows imperfections in the nanofabricated zones. Other defects, corroborated by a SEM image, are shown in fig. S1. The outermost rings of the zone plate (70 nm wide) are very well resolved. The pixel size is 18 nm. The total acquisition time for this image is 186 s, with a total dose of 2×10^9 photons.

Fig. 4. Reconstructed probe. (A) Color rendition of the complex-valued probe at the specimen plane. (B) The computed wavefield propagated back to the focal plane, situated 1.2 mm upstream. (C) A section of the probe wavefield along the propagation direction, as calculated from the data in (A). The dashed line, indicating the plane of (B), is at the waist of the wave distribution. (D) The squared amplitude of the Fourier transform of the probe. (E) Measured diffraction pattern of the probe without a specimen. This data, which was not used in the reconstruction, is in good agreement with the retrieved probe.



specimen. The amplitude component carries the absorption information, and the phase expresses the phase shift experienced by a wave when traversing the specimen. In the present case, the phase difference caused by the 1.0- μm -thick gold structure in the zones is measured to be about 0.67π , in very good agreement with the expected value of 0.65π . We note that a complex reconstruction carries the necessary information to reproduce any traditional microscopy arrangement. For instance, a differential phase contrast image, similar to Fig. 2, C and D, is simply given by the gradient of Fig. 3B. An example of a simulated phase contrast image is shown in fig. S1C.

The wavefield of the probe, which is retrieved at the same time as the object, is shown in Fig. 4A. The knowledge of both the phase and the amplitude of the wave gives the most complete information for subsequent analysis. Computed propagation of this wavefield shows that the specimen was placed 1.2 mm behind the focal plane and was thus illuminated with a slightly curved and diverging wavefront.

Unlike the few other known methods (11, 28), the probe reconstruction does not require any knowledge of the pupil of the Fresnel zone plate. In fact, it does not require a pupil plane. Probes formed with refractive (29) or reflective (30) optics can be equally well reconstructed, as well as unfocused probes formed with a mask. The door to a general wavefront characterization procedure appears to be even more widely open when one realizes the symmetry in the multiplicative relation between P and O in Eq. 1. Transferring the oversampling requirement to the object function placed downstream—for instance, by using a simple pinhole—allows the characterization of arbitrary large and extended regions of an incoming wavefield. In this wavefront-sensing configuration, what was the “probe” becomes the main object of interest. It can be the propagated wave perturbation from any specimen or optical device. This feature will be useful for the characterization of focusing devices to be used at future coherent x-ray light sources.

We have demonstrated an imaging technique that is fully compatible with STXM and has the high-resolution potential of CDI approaches. The reconstruction method removes the main difficulty of ptychography by retrieving the complex-valued image of both the specimen and the probe. The method is noninvasive, and radiation damage can be reduced by a combination of fast large-area scans with longer high-resolution imaging of regions of interest. The technique can be used with hard and soft x-rays, can be combined with other scanning methods such as fluorescence imaging, and can be extended to nano-diffraction mapping or nanospectroscopy. Higher coherent flux and improved focusing optics (31) should soon provide conditions for better-than-10-nm resolutions, making possible the imaging of the finest structures in state-of-the-art electronics devices or the macromolecular assemblies

in organic tissues. Future developments comprise extension of the method to 3D reconstructions of inorganic and organic specimens as a possible answer to the current limitations of diffraction microscopy (32).

References and Notes

1. J. Miao, P. Charalambous, J. Kirz, D. Sayre, *Nature* **400**, 342 (1999).
2. H. N. Chapman *et al.*, *Nat. Phys.* **2**, 839 (2006).
3. H. N. Chapman *et al.*, *J. Opt. Soc. Am. A* **23**, 1179 (2006).
4. G. J. Williams, M. A. Pfeifer, I. A. Vartanyants, I. K. Robinson, *Phys. Rev. Lett.* **90**, 175501 (2003).
5. J. Miao *et al.*, *Proc. Natl. Acad. Sci. U.S.A.* **100**, 110 (2003).
6. D. Shapiro *et al.*, *Proc. Natl. Acad. Sci. U.S.A.* **102**, 15343 (2005).
7. I. McNulty *et al.*, *Science* **256**, 1009 (1992).
8. S. Eisebitt *et al.*, *Nature* **432**, 885 (2004).
9. J. M. Rodenburg, R. H. T. Bates, *Philos. Trans. R. Soc. London Ser. A* **339**, 521 (1992).
10. P. Nellist, B. C. McCallum, J. M. Rodenburg, *Nature* **374**, 630 (1995).
11. H. N. Chapman, *Ultramicroscopy* **66**, 153 (1996).
12. J. M. Rodenburg, A. C. Hurst, A. G. Cullis, *Ultramicroscopy* **107**, 227 (2007).
13. J. M. Rodenburg *et al.*, *Phys. Rev. Lett.* **98**, 034801 (2007).
14. R. Hegerl, W. Hoppe, *Ber. Bunsenges. Phys. Chem* **74**, 1148 (1970).
15. G. Morrison, A. Gianoncelli, B. Kaulich, D. Bacescu, J. Kovac, in *Proceedings of the Eighth International Conference on X-ray Microscopy*, IPAP Conference Series **7**, 377 (2005).
16. B. Hornberger, M. Feser, C. Jacobsen, *Ultramicroscopy* **107**, 644 (2007).
17. C. Brönnimann *et al.*, *J. Synchrotron Radiat.* **13**, 120 (2006).
18. Materials and methods are available as supporting material on Science Online.
19. The validity of this relation, discussed in (18), depends on the thickness of the specimen, on the probe's depth of focus, and on the resolution of the reconstruction.
20. Measurements were carried at the coherent small-angle x-ray scattering (cSAXS) beamline of the Swiss Light Source at Paul Scherrer Institut.
21. At each point \mathbf{r}_j of the raster grid, assuming that O varies slowly within the illuminated region, the measured diffraction pattern can be approximated with $I_j(\mathbf{q}) \approx |O(\mathbf{r}_j)|^2 |\tilde{P}[\mathbf{q} - \nabla\phi(\mathbf{r}_j)]|^2$, where \tilde{P} is the Fourier transform of P . The specimen's transmission, $|O(\mathbf{r}_j)|^2$, is read from the overall attenuation of the signal, and the phase gradient, $\nabla\phi(\mathbf{r}_j)$, is seen as a position shift of the diffraction pattern on the detector.
22. J. M. Rodenburg, H. M. L. Faulkner, *Appl. Phys. Lett.* **85**, 4795 (2004).
23. H. M. L. Faulkner, J. M. Rodenburg, *Phys. Rev. Lett.* **93**, 023903 (2004).
24. V. Elser, *J. Opt. Soc. Am. A* **20**, 40 (2003).
25. V. Elser, I. Rankenburg, P. Thibault, *Proc. Natl. Acad. Sci. U.S.A.* **104**, 418 (2007).
26. In the Fraunhofer regime, the wave in the transverse plane at the exit of the specimen $\psi(\mathbf{r})$ is related to the intensity measurement by $I(\mathbf{q}) = |\tilde{\psi}(\mathbf{q})|^2$, where $\tilde{\psi}(\mathbf{q})$ is the 2D Fourier transform of $\psi(\mathbf{r})$. This equality constrains the amplitude of $\tilde{\psi}(\mathbf{q})$ but not its phase.
27. The best object and probe functions, given a set of views (ψ_1, ψ_2, \dots) are the solution of the coupled system $O(\mathbf{r}) = \frac{\sum_j P^*(\mathbf{r} - \mathbf{r}_j) \psi_j(\mathbf{r})}{\sum_j |P(\mathbf{r} - \mathbf{r}_j)|^2}$, $P(\mathbf{r}) = \frac{\sum_j O^*(\mathbf{r} + \mathbf{r}_j) \psi_j(\mathbf{r} + \mathbf{r}_j)}{\sum_j |O(\mathbf{r} + \mathbf{r}_j)|^2}$. More details on the algorithm are provided in (18).
28. H. M. Quiney, A. G. Peele, Z. Cai, D. Paterson, K. A. Nugent, *Nat. Phys.* **2**, 101 (2006).
29. C. Schroer *et al.*, *Appl. Phys. Lett.* **82**, 1485 (2003).
30. H. Mimura *et al.*, *Appl. Phys. Lett.* **90**, 051903 (2007).
31. K. Jefimovs *et al.*, *Phys. Rev. Lett.* **99**, 264801 (2007).
32. D. Sayre, *Acta Crystallogr. A* **64**, 33 (2008).
33. We wish to thank P. Kraft, E. F. Eikenberry, B. Henrich, and C. Brönnimann for the Pilatus detector commissioning and the ongoing support; K. Jefimovs for the fabrication of nanostructures; K. Nygard for producing the scanning electron microscopy (SEM) picture of the specimen; X. Donath for the technical support at the cSAXS beamline; and J. Rodenburg for introducing us to ptychography. This work was performed at the Swiss Light Source, Paul Scherrer Institut, Villigen, Switzerland. P.T. acknowledges financial support from the Fonds Québécois de la recherche sur la nature et les technologies (FQRNT).

Supporting Online Material

www.sciencemag.org/cgi/content/full/321/5887/379/DC1

Materials and Methods

Fig. S1

References

2 April 2008; accepted 13 June 2008

10.1126/science.1158573

Observations of Intergranular Stress Corrosion Cracking in a Grain-Mapped Polycrystal

A. King,^{1,2*} G. Johnson,^{1,2} D. Engelberg,¹ W. Ludwig,^{2,3} J. Marrow¹

Nondestructive three-dimensional mapping of grain shape, crystallographic orientation, and grain boundary geometry by diffraction contrast tomography (DCT) provides opportunities for the study of the interaction between intergranular stress corrosion cracking and microstructure. A stress corrosion crack was grown through a volume of sensitized austenitic stainless steel mapped with DCT and observed in situ by synchrotron tomography. Several sensitization-resistant crack-bridging boundaries were identified, and although they have special geometric properties, they are not the twin variant boundaries usually maximized during grain boundary engineering.

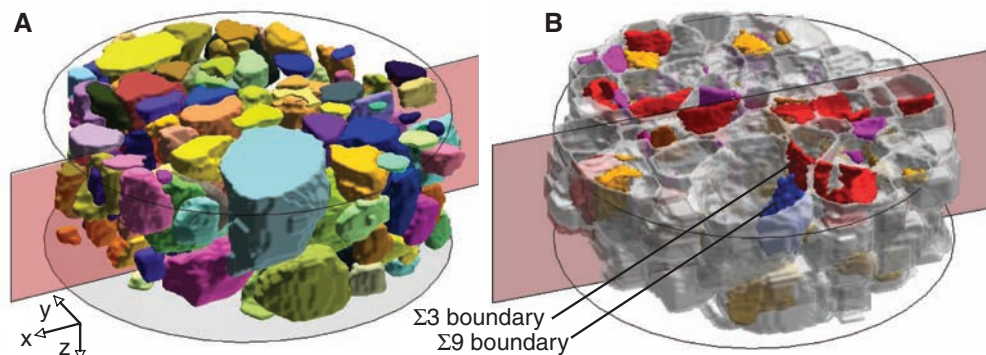
Intergranular stress corrosion cracking (IGSCC) is the progressive nucleation and growth of cracks by localized corrosion along the grain boundaries in metals in the presence of stress or

strain. Crack growth is driven by the inelastic deformation at the sharp crack tip. Thus, IGSCC is the result of the combination of susceptible material, critical environment, and sufficient mechanical driv-

ing force. It is a critical failure mechanism in some components of a power generation plant (1), where the cracking of austenitic stainless steels can result from the sensitization of certain grain boundaries after heat treatment (such as post-weld stress relief) or fast neutron irradiation in a nuclear plant.

Sensitization decreases the local resistance of grain boundaries to corrosion. Thermal sensitization is due to chromium carbide precipitation at the grain boundaries (2). The slow diffusing chromium is depleted in the region adjacent to the carbides, to a degree sufficient to substantially reduce the oxidation resistance. Chromium depletion at grain boundaries also occurs with irradiation damage (3), although point defect creation and

Fig. 1. Part of the 3D grain map obtained by DCT, including 169 grains (a total of 362 grains were mapped). The circumference of the sample is outlined, and the plane of the 2D section in Fig. 3 is also shown. (A) Grains colored using a RGB scale, according to their crystallographic orientation. (B) Low Σ CSL grain boundaries are shown in color: low-angle $\Sigma 1$, orange; $\Sigma 3$, red; $\Sigma 9$, blue; other boundaries $\Sigma \leq 29$, purple.



¹School of Materials, University of Manchester, Manchester M13 9PL, UK. ²European Synchrotron Radiation Facility, Grenoble, France. ³Matériaux: Ingénierie et Science, Institut National des Sciences Appliquées de Lyon, Villeurbanne, France.

*To whom correspondence should be addressed. E-mail: andrew.king@esrf.fr